# Analytical computation of magnetic field in coil-dominated superconducting quadrupole magnets based on racetrack coils*

Chuang Shen,[1,2] Yin-Shun Zhu,[2,†] and Fu-San Chen[2,3]

[1] *China Spallation Neutron Source, Institute of High Energy Physics, Chinese Academy of Sciences, 1 Zhongziyuan Road, Dongguan, Guangdong 523000, China,*

[2] *Institute of High Energy Physics, Chinese Academy of Sciences, 19B Yuquan Road, Beijing 100049, China*

[3] *University of Chinese Academy of Sciences, Beijing 100049, China*

Currently, three types of superconducting magnets are used in particle accelerators: cos2θ, CCT, and serpentine. However, all three coil configurations have complex spatial geometries, which make magnet manufacturing and strain-sensitive superconductor applications difficult. Compared with the three existing quadrupole coils, the racetrack quadrupole coil has a simple shape and manufacturing process, but there have been few theoretical studies. In this paper, the two-dimensional and three-dimensional analytical expressions for the magnetic field in coil-dominated racetrack superconducting quadrupole magnets are presented. The analytical expressions of the field harmonics and gradient are fully resolved and depend only on the geometric parameters of the coil and current density. Then, a genetic algorithm is applied to obtain a solution for the coil geometry parameters with field harmonics on the order of $10^{-4}$. Finally, considering the practical engineering needs of the accelerator interaction region, electromagnetic design examples of racetrack quadrupole magnets with high gradients, large apertures, and small apertures are described, and the application prospects of racetrack quadrupole coils are analyzed.

Keywords: Superconducting quadrupole magnet, racetrack coil, multipole field, genetic algorithm, magnetic design

## I. INTRODUCTION

With the development of superconducting magnet technology in particle accelerators, cos2θ coil and serpentine coil structures have been successfully applied to the final focus system in the interaction region. The cos2θ magnet structure is commonly used in the accelerator interaction regions. After decades of development, the cos2θ superconducting magnets have matured for theoretical guidance and engineering applications [1, 2]. The cos2θ coil is saddle-shaped in the longitudinal direction and fan-shaped in the cross section around the beam aperture, which simulates the distribution of the quadrupole coil current $I = I_0 cos(2\theta)$. The processing and manufacturing of cos2θ magnets requires winding systems, curing systems, assembly systems, and other related equipment. The magnet consists of coils, collars, and an iron yoke. The superconductor, spacer, and wedge were solidified as a solid whole after processing. Collars are used to provide pre-stress and fix the coil to form a self-supporting structure [3]. A small-aperture cos2θ superconducting quadrupole magnet, QD0, is the basic scheme for the final focus system in the CEPC interaction region [4, 5]. A large-aperture cos2θ quadrupole magnet, MQXF, is composed of $Nb_3Sn$ superconductors in the interaction region of the HL-LHC upgrade project [6, 7]. Serpentine winding, an innovation developed at BNL for direct-winding superconducting magnets, allows the winding of a coil layer of arbitrary multipolarity in one continuous winding process and considerably simplifies magnet design and production [8, 9]. A winding machine with multi-axis motion was used to wind each layer of the coil separately, and the four poles of each layer were wound simultaneously. Ultrasonic technology was used to heat the semicured glue and fix the superconductor in time. A low-temperature glue was brushed on the coil to hold it in place. After the low-temperature glue was cured, it was wrapped with a glass yarn on the outside to apply pre-stress, which eliminated the need for a extra pre-stress structure and reduced the magnet size. A serpentine quadrupole magnet was used for the BEPC-II Upgrade [10, 11], which was also proposed for manufacturing compact final focus magnets for the ILC.

With improvements in the machining accuracy of machine tools, CCT magnets have also become the focus of accelerator magnet research. The position coordinates of each turn of the superconductor in the CCT coil are determined by a parameter equation that is strictly arranged on the surface of the cylinder [12, 13]. The current density of the CCT quadrupole coil section also satisfies the cos2θ distribution and the multilayer coil skeleton structure can realize a combined functional magnet. According to the superconductor distribution, the CCT coil needs to slot the surface of the cylindrical skeleton using CNC machining or 3D printing technology, and then place the superconductors directly into the slot and fix it [14]. CCT quadrupole magnets are supported by a comprehensive theoretical foundation and have been used in a preliminary study of superconducting quadrupole magnets in the Fcc-ee interaction region [15].

With a further increase in the beam energy in a large particle collider, higher-gradient superconducting quadrupole magnets are required in the interaction region. A higher field gradient indicates that the superconductors need to carry more current. When the peak magnetic field in the coil exceeds 10 T, the mature low-temperature superconductor NbTi reaches its theoretical limit. The current-carrying capacity of the superconductor $Nb_3Sn$ with a higher critical magnetic field also

* This work was supported in part by the National Key Research and Development Program of China 2022YFA1603402 and in part by the National Natural Science Foundation of China under Contract 11875272

† Corresponding author, yszhu@ihep.ac.cn

decreases sharply. However, with an increase in the magnetic field, the critical current density of the high-temperature superconductor decreases slightly, which is a better choice for realizing high-gradient superconducting quadrupole magnets. High-temperature superconductors are more strain-sensitive than low-temperature superconductors and are unsuitable for cos2θ, CCT, and serpentine coils with complex spatial geometries. Therefore, a racetrack coil with a simple spatial shape and gentle bending is suitable for use in high-temperature superconductors. The above is an advantage of using racetrack coils for high-field magnets with a peak magnetic field greater than 10 T, for some low-field superconducting quadrupole magnets with a smaller peak magnetic field, considering the radiation damage and heating, a high-temperature superconductor is also a necessary choice to provide sufficient operating margins to ensure operating stability.

Iron-dominated and coil-dominated superconducting magnets are the two basic types. Owing to the iron pole saturation phenomenon, iron-dominated racetrack quadrupole magnets have a low magnetic field intensity, and the magnetic field quality is difficult to control, which cannot meet the requirements of large particle accelerators [16–20]. From this perspective, a coil-dominated racetrack quadrupole magnet is a reliable method for achieving an ultrahigh magnetic field gradient. Recently, studies have been conducted on coil-dominated racetrack quadrupole magnets. The US LHC Accelerator Research Program has completed the design and processing of racetrack superconducting magnets SQ01 and SQ02 using the superconductor $\mathrm{Nb_3Sn}$ and conducted quench tests [21, 22]. However, the research on coil-dominated racetrack quadrupole magnets is limited and requires further improvement. First, current research on racetrack quadrupole magnets is based on finite element software, which lacks the guidance of theoretical formulas such as the Cos2θ coil [23, 24]. Second, return coils are added to form racetrack coils, which increase the size of the magnet cross-section. Current distribution patterns are complex, causing difficulties in the design and manufacturing of magnets. [25, 26].

The focus of this study was a magnetic field numerical calculation algorithm for a coil-dominated racetrack quadrupole coil. First, the field harmonics and gradient analytical expressions of the two-dimensional racetrack quadrupole coil as a function of the geometric parameters and current density were derived based on the line current theory, coordinate transformation, and numerical integration. Second, a genetic algorithm is applied to obtain a solution for the coil geometry parameters with field harmonics of the order of $10^{-4}$. Subsequently, the three-dimensional analytical expressions of the high-order field harmonics in the racetrack quadrupole coil were obtained using the discrete summation algorithm. Combined with the finite element software, the accuracy of the numerical calculation algorithm was verified. Finally, combined with the practical engineering design requirements of accelerator magnets, electromagnetic designs of racetrack quadrupole magnets with high gradients, large apertures, and small apertures are described, and the application prospects of racetrack quadrupole coils are analyzed.

## II. NUMERICAL CALCULATION ALGORITHM FOR TWO-DIMENSIONAL RACETRACK QUADRUPOLE COIL MAGNETIC FIELD

According to the complex formalism, the line current $I$ in the position $z_0 = x_0 + iy_0$ generates a magnetic field $B(z) = B_y(z) + iB_x(z)$ in the position $z = x + iy$, which reads [27]

$$B(z) = \frac{I\mu_0}{2\pi(z - z_0)} \tag{1}$$

where $u_0$ is the permeability of the vacuum. Multipole field components in the aperture generated by line current $I$ at position $z_0 = x_0 + iy_0 = r_0 e^{i\theta_0}$ are

$$\begin{aligned} B_n &= -\frac{I\mu_0}{2\pi}\frac{R_{ref}^{n-1}}{r_0^n}\cos n\theta_0 \\ A_n &= \frac{I\mu_0}{2\pi}\frac{R_{ref}^{n-1}}{r_0^n}\sin n\theta_0 \end{aligned} \tag{2}$$

$R_{ref}$ is the reference radius of the good region, determined by the clear region of the beam. Normal and skew quadrupole magnets are the two basic quadrupole types. A normal quadrupole magnet was obtained by rotating a skew quadrupole magnet by 45°. The multipole field components in the aperture generated by the rotating line current $I'$ at position $z_0' = z_0 e^{-i\frac{\pi}{4}} = r_0 e^{i(\theta_0 - \frac{\pi}{4})}$ are

$$\begin{aligned} B_n' &= -\frac{I\mu_0}{2\pi}\frac{R_{ref}^{n-1}}{r_0^n}\cos n(\theta_0 - \frac{\pi}{4}) \\ A_n' &= \frac{I\mu_0}{2\pi}\frac{R_{ref}^{n-1}}{r_0^n}\sin n(\theta_0 - \frac{\pi}{4}) \end{aligned} \tag{3}$$

For the high-order field harmonics of the magnetic field, $n$ in Eq. (3) equals *4N-2, N=1, 2, 3…*. The Eq. (3) can be written as

$$A_n' = -\frac{I\mu_0}{2\pi}\frac{R_{ref}^{n-1}}{r_0^n}\sin\left((2N-1)\frac{\pi}{2} - (4N-2)\theta_0\right) \tag{4}$$

When $N$ is odd, $n$= *2, 10, 18…*

$$\begin{aligned} A_n' &= -\frac{I\mu_0}{2\pi}\frac{R_{ref}^{n-1}}{r_0^n}\cos\left((4N-2)\theta_0\right) \\ &= -\frac{I\mu_0}{2\pi}\frac{R_{ref}^{n-1}}{r_0^n}\cos(n\theta_0) \\ &= B_n \end{aligned} \tag{5}$$

When $N$ is even, that is, $n$ = *6, 14, 22…*

$$A'_n = \frac{I\mu_0}{2\pi}\frac{R_{ref}^{n-1}}{r_0^n}\cos\left(\left(4N-2\right)\theta_0\right) \\ = \frac{I\mu_0}{2\pi}\frac{R_{ref}^{n-1}}{r_0^n}\cos\left(n\theta_0\right) \\ = -B_n \tag{6}$$

According to Eq. (5), and Eq. (6),

$$a'_n = \frac{A'_n}{A'_2} = \begin{cases} \frac{B_n}{B_2} = b_n, & n = 10, 18\ldots \\ \frac{-B_n}{B_2} = -b_n, & n = 6, 14, 22\ldots \end{cases} \tag{7}$$

Among the high-order field harmonics $a_6$, $a_{10}$ and $a_{14}$, a negative sign must be added to harmonics $a_6$ and $a_{14}$ in the transformation from a skew quadrupole magnet to a normal quadrupole magnet [28].

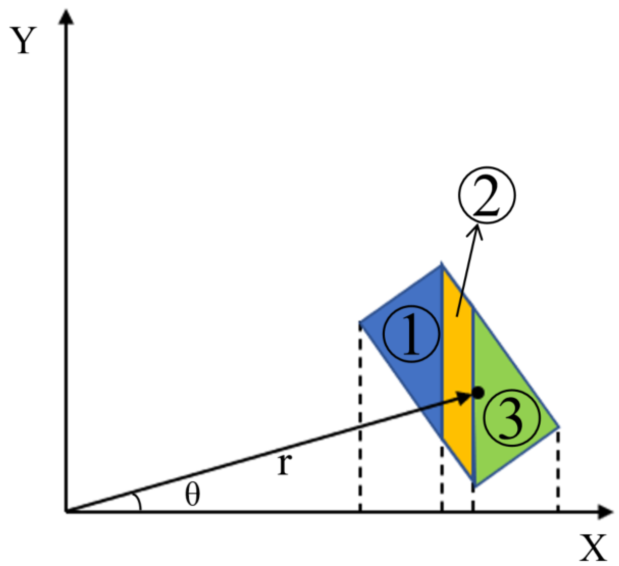


Fig. 1. Schematic of current distribution in 0-45° quadrant of normal racetrack quadrupole coil. The three areas marked with different colors and numbers in the figure indicate that the definitive integral in rectangular coordinates needs to be solved in three regions.

There are two ideas for the numerical calculation of a two-dimensional magnetic field: complex representation [29] and real representation. The real representation is also the method used in this study. Fig. 1 shows the current distribution diagram of a normal racetrack quadrupole coil in the quadrants from 0° to 45°. The coil cross-sectional distribution makes the integration operation extremely difficult in coordinate systems. Although normal quadrupole magnets are commonly used in accelerator-focusing systems, a skew quadrupole magnet was considered as our research object to facilitate the integral calculation process in the cartesian coordinate system. When the skew quadrupole magnet is rotated by 45° to form a normal quadrupole magnet, the multipole field also changes from the skew field $A_n$ to the normal field $B_n$, and such a change only affects the positive or negative signs of the field harmonics. Eq. (7) deduces the conversion relationship between the high-order field harmonics of the normal and skew quadrupole coils:

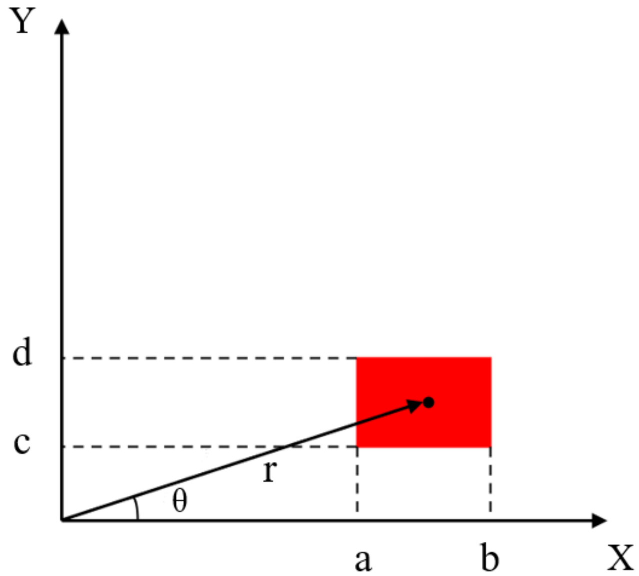


Fig. 2. Schematic of current distribution in 0-45° quadrant of skew racetrack quadrupole coil.

Fig. 2 shows the current distribution diagram of the skew racetrack quadrupole coil in the quadrant ranging from 0° to 45°. A parameter definition for the current block is presented. To derive the total field produced by the current block, the multipole field component expressions in polar coordinates were transformed into cartesian coordinates. The transformation formulas for the two coordinate systems are as follows:

$$r = \sqrt{x^2+y^2} \\ \theta = arctan\left(\frac{y}{x}\right) \tag{8}$$

From Eq. (8), the multipole field components generated by the differential unit of the rectangular block are

$$dA_{n(block-abcd)} = \frac{\mu_0 j}{2\pi}\frac{R_{ref}^{n-1}}{\left(x^2+y^2\right)^{\frac{n}{2}}} \\ \times \sin n\left(arctan\left(\frac{y}{x}\right)\right)\ dydx \tag{9}$$

where $j$ is the current density of the coil block. The multipole field components in the aperture generated by the rectangular current block shown in Fig. 1 can be calculated as

$$A_{n(block-abcd)} = \int_a^b\int_c^d \frac{\mu_0 j}{2\pi}\frac{R_{ref}^{n-1}}{\left(x^2+y^2\right)^{\frac{n}{2}}} \\ \times \sin n\left(arctan\left(\frac{y}{x}\right)\right) dydx \tag{10}$$

According to Eq. (10), each order multipole field $A_n$ of the entire racetrack quadrupole coil is obtained. For example, analytical expressions for the quadrupole field component and field gradient are obtained. Other analytical expressions of multipole fields $A_6$ and $A_{10}$ are listed in the Appendix.

$$
\begin{aligned}
A_2 &= \frac{2\mu_0 j R_{ref}}{\pi} \ln \frac{\left(a^2+d^2\right)\left(b^2+c^2\right)}{\left(a^2+c^2\right)\left(b^2+d^2\right)} \\
G &= \frac{A_2}{R_{ref}} = \frac{2\mu_0 j}{\pi} \ln \frac{\left(a^2+d^2\right)\left(b^2+c^2\right)}{\left(a^2+c^2\right)\left(b^2+d^2\right)}
\end{aligned} \tag{11}
$$

The relative field harmonics normalized to the main quadrupole field component are defined as $a_n = A_n/A_2$. Then, the high-order field harmonics $a_6$, $a_{10}$ and $a_{14}$ can be derived. These analytical expressions contain four parameters: $a$, $b$, $c$, and $d$.

In the analytical expressions, parameter $a$ represents the x-axis coordinate value corresponding to the left side of the rectangular current block, which is directly related to the aperture of the racetrack superconducting quadrupole coil. Therefore, after reserving the space required by the coil support structure, the parameter $a$ is the first determined variable. According to the aperture of the quadrupole coil in the CEPC interaction region, the parameter $a$ is set to be 0.02 m. The reference radius $R_{ref}$ was set as 0.0098 m [30, 31].

Subsequently, the relationship between the high-order field harmonics and other parameters was further studied. Among the high-order field harmonics of superconducting quadrupole magnets, the systematic harmonics $a_6$, $a_{10}$ and $a_{14}$ have been the main research objects. Field harmonics $a_6$ as functions of the coil parameters are shown in Fig. 3. The different layered structures in the z direction are caused by the different parameters $b$. Different parameters $c$ and $d$ result in significant changes in the surface of the high-order field harmonics $b_6$. The intersection of the high-order field harmonics surface and z=0 plane indicates that $b_6$ is equal to zero. At this time, the parameters $b$, $c$, and $d$ corresponding to each point on the intersection line are the solutions.

Similarly, as shown in Fig. 3, the value range of the high-order field harmonics $a_{10}$ exhibits a small change, and most results are within the design requirements. The intersection of the high-order field harmonics surface and z=0 plane indicates that $b_{10}$ is equal to zero. As shown in Fig. 3, harmonics $a_{14}$ are extremely small over the entire solution area. The intersection of the high-order field harmonics surface and z=0 plane indicates that $b_{14}$ is equal to zero.

From an analysis of the high-order field harmonics of $a_6$, $a_{10}$, and $a_{14}$, it can be observed that $a_{14}$ is relatively small. Thus, $a_6$ and $a_{10}$ are the key to this study. Under the condition that parameters $a$, $b$, and $c$ are determined, the relationship between parameter $d$ and the high-order field harmonics is studied. $a_6$ and $a_{10}$ as functions of the coil parameters are shown in Fig. 4. All the points in the solution set regions 1 and 2 meet the requirement that the high-order field harmonics be less than $5 \times 10^{-4}$, which can be used as the solution of the model. However, such a graphical solution is complicated, and a coil pole composed of a single-block region causes a large excitation current in the superconducting cable.

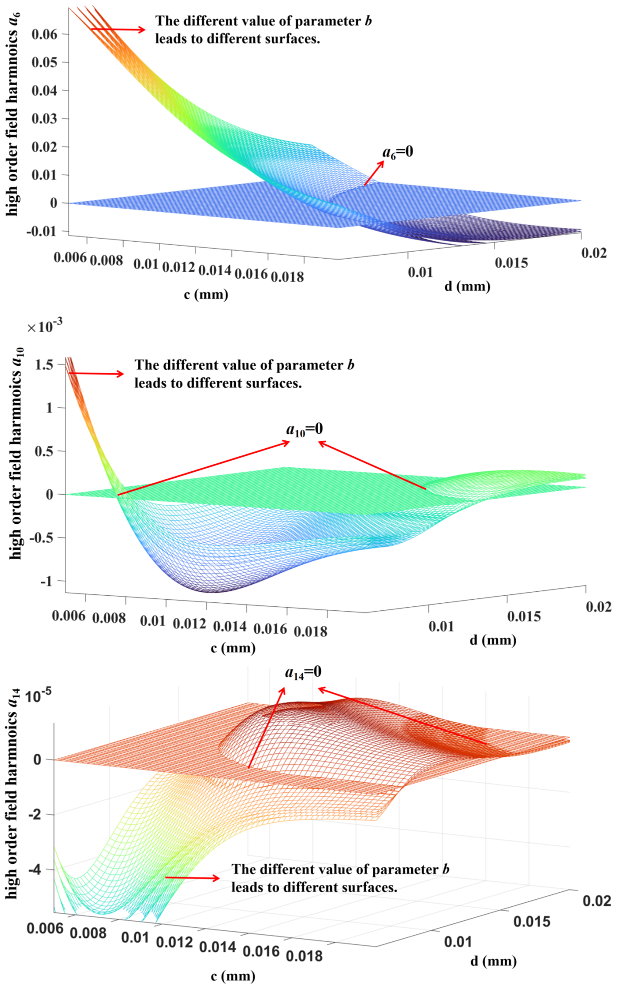

Fig. 3. High-order field harmonics distribution of racetrack quadrupole coil

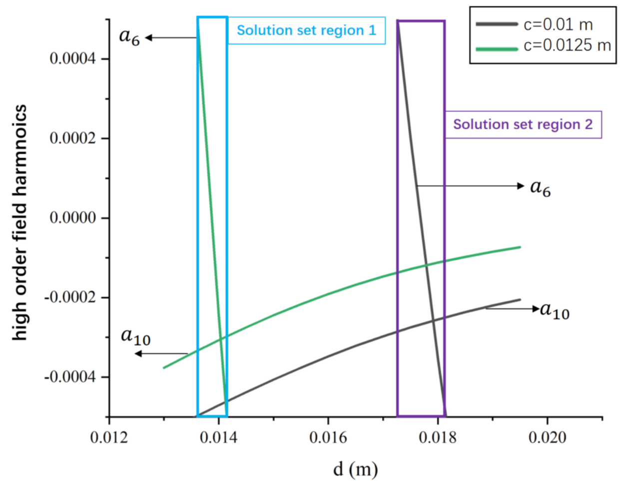

Fig. 4. Distribution of high-order field harmonics under the same parameters $a$, $b$, and $c$.

Therefore, the model must be further optimized to improve the efficiency of the solution and reduce the difficulty in magnet design and manufacturing. Increase the current blocks in each pole and improve the ability to adjust the magnetic field quality. Meanwhile, the solution method was optimized, the efficiency of the model solution was enhanced, and the practical application value of the racetrack coil analysis algorithm was improved.

To make the design of the theoretical model more suitable for actual situations and increase the adjustment ability of the quadrupole coil, a double-layer quadrupole coil composed of two blocks was used in the theoretical model. A double-layer racetrack quadrupole coil is shown in Fig. 5. For the range 0–45° in the first quadrant, the two rectangular blocks have the following constraints: $0 < c_1 < d_1 < a_1 < b_1$ and $0 < c_2 < d_2 < a_2 < b_2$. To ensure that the two rectangular blocks do not overlap, we add the following constraint $a_2 > b_1$:

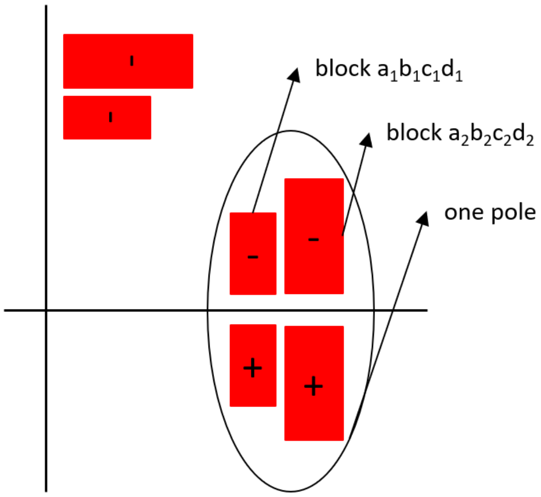


Fig. 5. Racetrack quadrupole coil with two blocks in each pole.

According to Eq. (10), the high-order field harmonics of the racetrack quadrupole coil consisting of two blocks were obtained:

$$\begin{aligned} a_{n-blocks} &= \frac{A_{n-blocks}}{A_{2-blocks}} \\ &= \frac{A_{n-block\ a_1b_1c_1d_1} + A_{n-block a_2b_2c_2d_2}}{A_{2-block\ a_1b_1c_1d_1} + A_{2-block a_2b_2c_2d_2}} \end{aligned} \tag{12}$$

According to the design requirements, the following expression can be obtained:

$$\begin{cases} a_6 = \dfrac{A_{6-block\ a_1b_1c_1d_1} + A_{6-block a_2b_2c_2d_2}}{A_{2-block\ a_1b_1c_1d_1} + A_{2-block a_2b_2c_2d_2}} \\ a_{10} = \dfrac{A_{10-block\ a_1b_1c_1d_1} + A_{10-block a_2b_2c_2d_2}}{A_{2-block\ a_1b_1c_1d_1} + A_{2-block a_2b_2c_2d_2}} \\ G = \dfrac{A_{2-block\ a_1b_1c_1d_1} + A_{2-block a_2b_2c_2d_2}}{R_{ref}} \end{cases} \tag{13}$$

Eq. (13) shows a complex set of high-order field harmonics and gradients. Based on previous research, it can be found that the high-order field harmonics $a_{14}$ are small compared to $a_6$ and $a_{10}$. Therefore, the high-order field harmonics $a_{14}$ are not considered for the time being, and the three physical quantities $a_6$, $a_{10}$, and gradient $G$ are used as the objective function. Based on the characteristics of the model, this is a multiobjective optimization problem. Traditional methods to deal with multiobjective optimization (MOO) problems usually convert such multiobjective problems into single-objective optimizations by formulating some forms of cost functions or by converting some objectives into constraints. However, it can be extremely difficult to provide a suitable weighting factor for determining preferences, and it is challenging to place proper constraints in engineering practice. Several multiobjective evolutionary algorithms (MOEAs) have been proposed to address this issue [32]. In this study, the NSGA2 genetic algorithm (belonging to MOEAs) based on the pymoo platform in Python was used to solve the multiobjective optimization model.

The calculation model of the genetic optimization algorithm is based on the biological evolution process of Darwin's genetic selection and natural elimination and is a search algorithm that embodies biological genetics and the natural law of survival of the fittest. All individuals in the population are considered objects, and a coded parameter space is randomly and efficiently searched using selection, crossover, and mutation genetic operations. The initial population of the parameter coding, fitness function, genetic operation, and control parameters constitute the core content of the genetic algorithm [33]. The focus of this study was the numerical calculation of the magnetic field of the racetrack quadrupole coil. The genetic algorithm is not the focus of our research; it is only a means to obtain the optimal layout of the coil. Therefore, the Python database was used to directly call NSGA2, Problem, Minimize, and other function modules, and to modify some parameters according to the problem to achieve our goal.

In the solution model, the model characteristics were specified before using the optimization algorithm to solve the problem. The distance from the inside of the coil to the origin was 0.075 m, and the distance from the outside of the coil to the origin was 0.112 m. Two layers of racetrack coils were arranged between 0.075 and 0.112 m. The reference radius of the quadrupole coil was 0.050 m. These parameters are determined by the accelerator physics, magnet structure, and superconductors. As shown in Fig. 6, where each red ball represents a solution. It is not difficult to conclude that many noninferior solutions can be obtained using the genetic algorithm.

In the two-dimensional image shown in Fig. 6, noninferior solutions were screened according to the requirements. There are two points at which the high-order field harmonics $a_6$ and $a_{10}$ simultaneously satisfy the requirements of $5 \times 10^{-4}$ at the same time. Considering the influence of the gradient, the optimal solutions are listed in Table 1.

Using the genetic algorithm, considering the limitations of space size, some solutions satisfying the conditions were

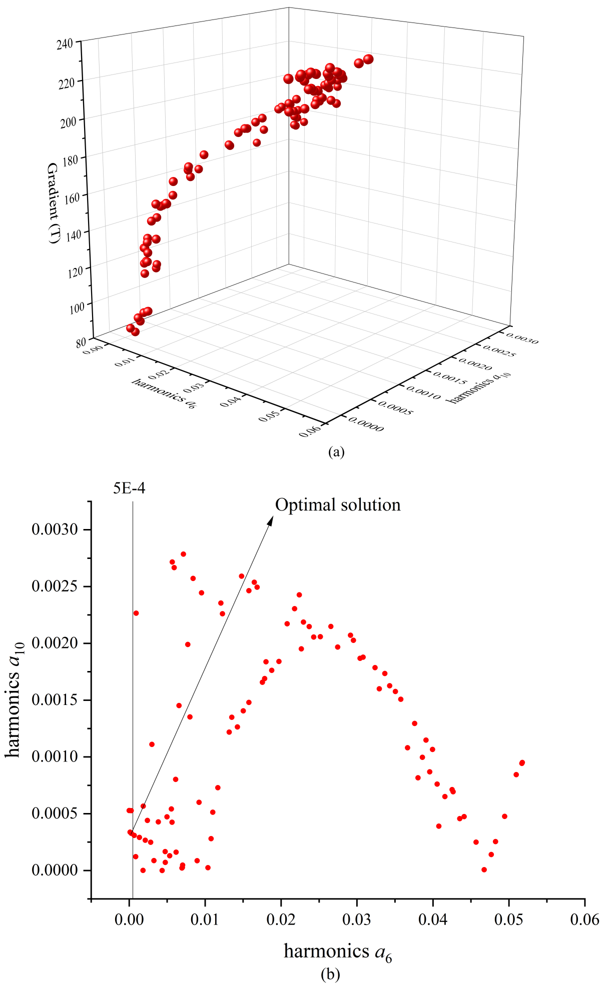


Fig. 6. Genetic algorithm solution results

found. According to the solution results of the analytical calculation method, a quadrupole model with the same coil parameters was established in the ROXIE software. A comparison between the results of the analytical method and the Finite Element Method is also shown in Table 1. The results of the analytical and finite element methods are in good agreement. The values in parentheses in the FEM results are the simulation results of the corresponding normal quadrupole coils, which also prove the correctness of the relationship between the high-order field harmonics of the normal quadrupole coil and the skew quadrupole coil deduced above.

By comparing the calculations of the analytical method with the finite element calculations, it was found that the calculation speed of the theoretical formula was faster. Furthermore, when the finite element method searches for an optimal solution, the initial value, search range, and search step length of each parameter are required. This is the process of local optimization near the initial value. If the initial value is unreasonable, the global optimal solution can easily be missed. However, the genetic algorithm is a process of global optimization, and it does not depend on the initial value [34, 35]; only the parameter range is required to find the optimal solution. The genetic algorithm only requires a few seconds to determine the optimal solution. Therefore, the method of using the genetic algorithm to find the optimal solution is more reliable and less time-consuming than the finite element method. Finally, according to the different application environments of the quadrupole coil, the genetic algorithm was used to obtain the optimal solution of the theoretical formula under different constraints. The theoretical formula-solving method is more flexible and convenient than the finite element method.

TABLE 1. Comparison of the analytical and FEM results.

| Parameter | Analytical results | FEM results |
|---|---|---|
| | $a_1$=0.075 | $a_2$=0.094 |
| Block $(\mathrm{m})$ | $b_1$=0.093 | $b_2$=0.112 |
| | $c_1$=0.0569394 | $c_2$=0.02924927 |
| | $d_1$=0.0739649 | $d_2$=0.07481863 |
| Current density $(\mathrm{A/mm^2})$ | 1044 | 1044 |
| Gradient $(\mathrm{T/m})$ | -123.4 | -123.4 |
| $a_6(10^{-4})$ | -2.854 | -2.867 (2.867) |
| $a_{10}(10^{-4})$ | -3.264 | -3.263 $(-3.263)$ |
| $a_{14}(10^{-4})$ | -0.118 | -0.118 (0.118) |

## III. NUMERICAL CALCULATION ALGORITHM FOR THREE-DIMENSIONAL RACETRACK QUADRUPOLE COIL MAGNETIC FIELD

The design of superconducting magnets can not only consider the cross-sectional magnetic field but also the magnetic field at the end of the magnet, which is very important and the most complicated and difficulty in the numerical calculation of the three-dimensional magnetic field. The surface of the racetrack quadrupole coil is a regular plane and a cylinder that does not contain a complex spatial geometry. The end of the coil is illustrated in Fig. 7. The end coil can be regarded as the intersection of a plane and a cylinder. The equations for the plane and the cylinder are as follows:

$$\begin{aligned} F\left(x,y,z\right) &= x = x_0 \\ G\left(x,y,z\right) &= y^2 + \left(z - L_s\right)^2 = R^2 \end{aligned} \tag{14}$$

where $F(x,y,z)$ is the plane where the coil is located, $G(x,y,z)$ is the cylindrical surface, $L_s$ is half the length of the straight-line segment of the coil, and $R$ is the bending radius of the coil.

The current direction in the conductor at the end of the coil is not parallel to the z-axis; therefore, to calculate the magnetic field generated by the end coil, it is necessary to calculate the angle between the current and z-axis directions.

The normal vectors of plane $F$ and cylinder $G$ are

$$\begin{aligned} \vec{n_1} &= \left(\frac{\partial F}{\partial x}, \frac{\partial F}{\partial y}, \frac{\partial F}{\partial z}\right) = (1,0,0) \\ \vec{n_2} &= \left(\frac{\partial G}{\partial x}, \frac{\partial G}{\partial y}, \frac{\partial G}{\partial z}\right) = (0,2y,2z-2L_s) \end{aligned} \tag{15}$$

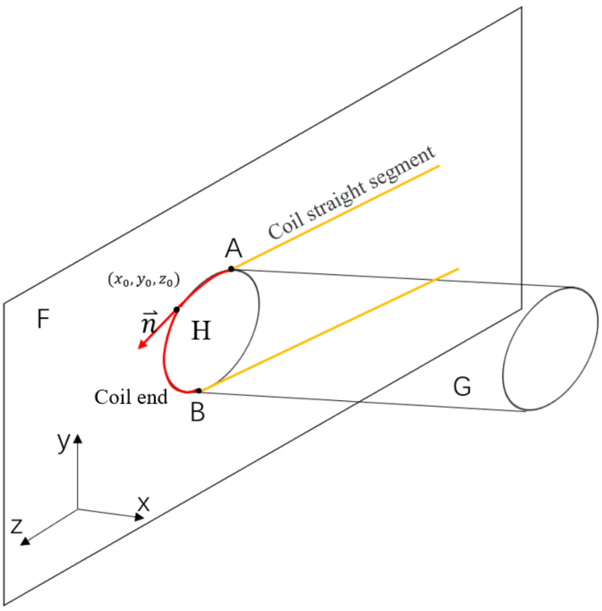


Fig. 7. Intersection of three-dimensional racetrack coil end.

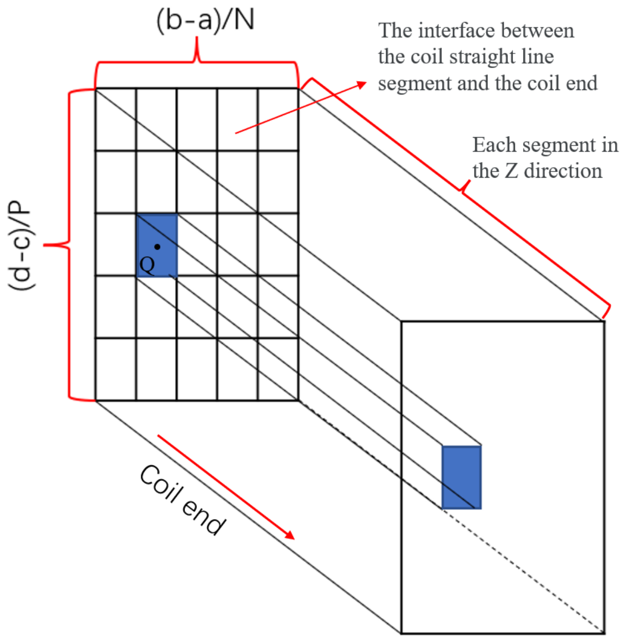


Fig. 8. Discrete method of three-dimensional racetrack coil end.

The tangent vector of any point Q at the intersection AB is

$$\vec{n} = \vec{n_1} \times \vec{n_2} = (0, 2L_s - 2z, 2y) \tag{16}$$

The cosine of the angle between the current direction and the z-axis in the conductor can be obtained from the tangent vector.

$$cos\alpha = \frac{\vec{n} \cdot \vec{e_z}}{|n|} = -\frac{2y}{\sqrt{(2L_s - 2z)^2 + (2y)^2}} \tag{17}$$

As shown in Fig. 8, the coil ends are discretized. The x-axis is discretized into N parts, where each part is $L_N = \frac{b-a}{N}$, and the y-axis is discretized into P parts, where each part is $L_P = \frac{d-c}{P}$. M were dispersed along the z-axis. As the bending radius of the coil end is related to the number of parts dispersed along the y-axis, the length of the $j$-th part on the y-axis after dispersion along the z-axis is $L_K = \frac{c + \frac{d-c}{2P}(2j-1)}{M}$.

To calculate the included angle between each end conductor and the z-axis, the Q coordinates of the center point of the initial cross-section of the $i$-th conductor on the x-axis, the $j$-th conductor on the y-axis, and the $k$-th conductor on the z-axis are as follows:

$$\begin{aligned} x_{i,j,k} &= a + \frac{b-a}{2N}(2i-1) \\ z_{i,j,k} &= L_S + \frac{c + \frac{d-c}{2P}(2j-1)}{M}(k-1) \\ y_{i,j,k} &= \sqrt{\left(c + \frac{d-c}{2P}(2j-1)\right)^2 - (z - L_S)^2} \end{aligned} \tag{18}$$

According to the multipole field component expressions of each straight conductor, high-order field harmonics of the integrated magnetic field generated by the $i$-th, $j$-th, and $k$-th conductor segments can be obtained [27].

$$\begin{aligned} (BL)_{n,(i,j,k)_{end}} &= -\frac{\mu_0 I L_K R_{\text{ref}}^{n-1} \cos\alpha_{i,j,k} \cos n\theta}{2\pi r_0^n} \\ (AL)_{n,(i,j,k)_{end}} &= \frac{\mu_0 I L_K R_{\text{ref}}^{n-1} \cos\alpha_{i,j,k} \sin n\theta}{2\pi r_0^n} \end{aligned} \tag{19}$$

For the straight coil section, the current in the conductor is parallel to the z-axis, that is, $\alpha$=0; therefore, the above formula is also applicable to the straight section coil, and the total integrated magnetic field of the racetrack coil is the superposition of the integrated magnetic fields generated by each discrete conductor segment.

$$\begin{aligned} B_{n,coil} &= \sum_{i=1}^{N}\sum_{j=1}^{P}\sum_{k=1}^{M}(BL)_{n,(i,j,k)end} + (BL)_{n,straight} \\ A_{n,coil} &= \sum_{i=1}^{N}\sum_{j=1}^{P}\sum_{k=1}^{M}(AL)_{n,(i,j,k)end} + (AL)_{n,straight} \end{aligned} \tag{20}$$

$B_{n,coil}$ and $A_{n,coil}$ are the $n$ order normal and skew components of the total integrated magnetic field, respectively. For normal and skew quadrupole coils, the relative magnetic fields $b_n$ and $a_n$ can be described as follows:

$$b_n = \frac{B_{n,\text{ coil}}}{A_{2,\text{ coil}}} \times 10^4, \quad a_n = \frac{A_{n,\text{ coil}}}{A_{2,\text{ coil}}} \times 10^4 \tag{21}$$

According to the above analysis, the analytical expressions of the high-order field of the three-dimensional coils can be obtained. A three-dimensional coil layout with smaller high-order field harmonics of the integrated magnetic field can be determined by adjusting the length of the straight-line segment. The length of the straight-line segment in the positive direction of the inner coil was 1075 mm, and the bending radius of the end was the parameter $c_1$; that is, the end shape was a regular semicircle. The length of the straight line in the positive direction of the outer coil was 1000 mm, and the bending radius of the end was parameter $c_2$. The three-dimensional coil model is solved using the discrete summation method. The number of discrete coils in the x-,y-, and z-directions affects the calculation accuracy. Combined with the performance of the computer and the accuracy of the model solution, the following discrete copies were determined: The discrete numbers of inner and outer coils in the x-direction were 585 and 576, respectively, with a length of 0.031 mm. The discrete numbers of the inner and outer coils in the y-direction were 553 and 1457, respectively, and the length of each part was 0.031 mm. The number of discrete parts of the inner coil along the z-axis was 370. Owing to the inconsistent lengths of the coil end, the minimum part length is 0.154 mm, the maximum part length is 0.2 mm, and the number of discrete parts of the outer coil on the z-axis is 187, the minimum part length is 0.156 mm, and the maximum part length is 0.4 mm.

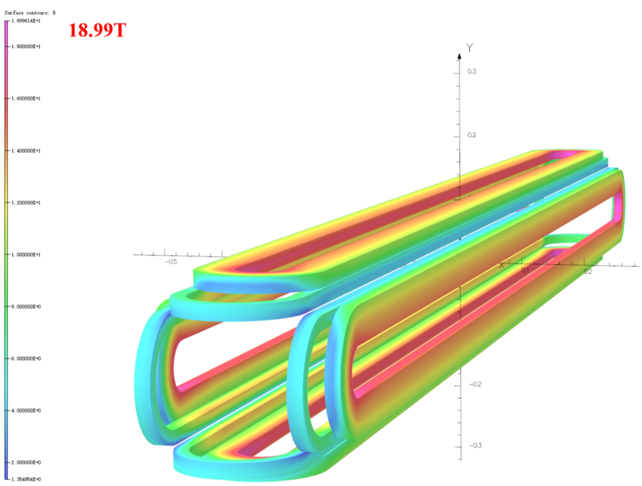


Fig. 9. Magnetic field analysis of OPERA three-dimensional coil model.

The numerical results of the magnetic field calculation for the whole three-dimensional coil can be obtained by writing a code to calculate the discrete accumulation of the magnetic field. Racetrack quadrupole coils were constructed directly using the racetrack module in OPERA-3D and ROXIE. The high peak magnetic field at the end of the three-dimensional coil is caused by the multiturn cable winding, which can be reduced by grouping the cables and adjusting the length of the straight segments. Fig. 9 shows the calculation model of OPERA, and Table 2 compares the results of the analytical algorithm, OPERA, and ROXIE for the high-order field harmonics calculation. The difference between the 12-pole magnetic-field component results obtained using the analytical formula and the software calculation results was three parts per million. The difference between the 20-pole magnetic field component and 28-pole magnetic field components is small, which proves the feasibility of the three-dimensional magnetic field numerical calculation algorithm.

TABLE 2. Calculation results of the three-dimensional algorithm for racetrack quadrupole coil.

| Field harmonics | Analytical results | OPERA | ROXIE |
|---|---|---|---|
| $a_6(10^{-4})$ | 0.385 | 0.406 | 0.419 |
| $a_{10}(10^{-4})$ | -3.060 | -3.056 | -3.056 |
| $a_{14}(10^{-4})$ | -0.100 | -0.098 | -0.099 |

## IV. PRELIMINARY ELECTROMAGNETIC DESIGN OF RACETRACK QUADRUPOLE MAGNETS

Through a theoretical study of racetrack quadrupole coils, the geometric parameters of ideal racetrack coils satisfying physical requirements were obtained. The parameters $a_1$, $b_1$, $c_1$, $d_1$, $a_2$, $b_2$, $c_2$, $d_2$ for the skew racetrack quadrupole coil are listed in Table 1. Based on the conversion of the normal and skew quadrupoles, the vertex coordinates of the two blocks in the skew quadrupole coil were rotated by 45° to become the vertex coordinates of the two blocks in the normal quadrupole coil. Rectangular superconducting cables are required to complete the block filling. Because of the influence of the superconducting cable insulation layer, the coil parameters must be fine-tuned during the electromagnetic design process.

The electromagnetic design of the racetrack quadrupole magnet was performed using ROXIE software. Table 3 lists the design requirements of a superconducting racetrack quadrupole magnet.

TABLE 3. Design requirements of the large-aperture superconducting quadrupole magnet.

| Parameters | Value |
|---|---|
| The inner radius of the quadrupole coils | 75 mm |
| Field gradient | 132 T/m |
| Reference radius | 50 mm |
| High order field harmonics | $\leq 5 \times 10^{-4}$ |

The double-layer normal racetrack coil structure is illustrated in Fig. 10. The width of the cable was 18 mm, and the thickness was 1.5 mm. The inner layer of the coil had 11 turns of superconducting cables and the outer layer had 28 turns of superconducting cables. The peak field of the coil is 16.33 T. The calculated high-order field harmonics were within $3 \times 10^{-4}$.

According to the particularity of the superconducting racetrack quadrupole coil, a bladder support structure was

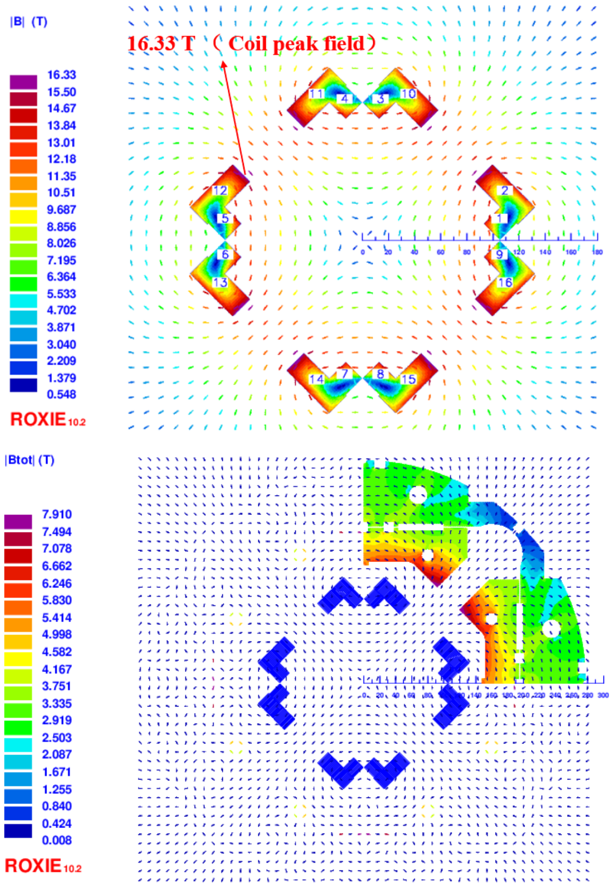


Fig. 10. Calculation model of large-aperture and high-gradient racetrack quadrupole coil

adopted, as shown in Fig. 10. To adjust the magnetic field quality and form a reliable pre-stress structure, the cross-section of the iron yoke is divided, slotted, and perforated [36, 37]. The simulation results are presented in Table 4. With the addition of an external iron yoke, the magnetic field gradient increased to 132 T/m, and the peak field in the coil reached 17.23 T. The high-order field harmonics $b_6$ change in the positive direction. By adjusting the coil parameters, the absolute value of the high-order field harmonics $b_6$ remained within $4 \times 10^{-4}$ after adding the iron yoke. When the magnetic field reaches 15-17 T, the current-carrying capacity of low-temperature superconductors is significantly reduced. Using a high-temperature superconductor is an effective method of achieving high gradients [38, 39].

TABLE 4. Calculation results of large-aperture and high-gradient racetrack quadrupole coil.

| Parameters | Coil | Coil with iron |
|---|---|---|
| Current density in strand | $1166\ \mathrm{A/mm^2}$ | |
| Field gradient | $122.0\ \mathrm{T/m}$ | $132.0\ \mathrm{T/m}$ |
| Peak field in coil | 16.33 T | 17.23 T |
| $a_6(10^{-4})$ | 2.103 | 3.855 |
| $a_{10}(10^{-4})$ | -2.825 | -2.633 |

In the next example of a small-aperture racetrack magnet, a racetrack quadrupole coil was applied to complete the design of the superconducting quadrupole magnet QD0 in the CEPC interaction region, and the CEPC adopted a double-ring collision mode [40]. There were two RF cavities [41, 42] and two interaction points on the main ring. Double-aperture conventional electromagnets were used in the main ring [43], and superconducting quadrupole magnets with high gradients and small apertures were used in the interaction region [44]. The design requirements of quadrupole magnet QD0 are listed in Table 5.

TABLE 5. Design requirements of small-aperture and high-gradient racetrack quadrupole coil.

| Parameters | Value |
|---|---|
| The inner radius of the quadrupole coils | 20 mm |
| Field gradient | $136\ \mathrm{T/m}$ |
| Reference radius | 9.8 mm |
| High order field harmonics | $\leq 5 \times 10^{-4}$ |

The cross-sectional layout of the coil obtained through parameter optimization is shown in Fig. 11. The width of the cable was 3.5 mm and the thickness was 1.5 mm. Each pole had 12 turns of superconducting cable, and the current density in the strands was $942.8\ \mathrm{A/mm^2}$. The high-order field harmonics are all within $3 \times 10^{-4}$. To enhance the magnetic field gradient, we added an iron shell to the coil. The inner edge of the iron is a regular octagon. The radius of the inner tangent circle of the octagon is 35 mm, and the outer radius of the iron shell is 54 mm.

Compared with the values of the quadrupole coils without an iron yoke in Table 6, when the iron yoke was added, the field harmonics increased slightly but were still within $3 \times 10^{-4}$. The field gradient was $136\ \mathrm{T/m}$. Superconducting magnets in the interaction region are affected by radiation from the particle beam. Considering the stability of the superconducting magnet, a small-aperture, high-gradient quadrupole magnet can also be designed with a high-temperature superconductor to leave an ample margin.

TABLE 6. Calculation results of large-aperture and high-gradient racetrack quadrupole coil.

| Parameters | coil | coil with iron |
|---|---|---|
| Current density in strand | $942.8\ \mathrm{A/mm^2}$ | |
| Field gradient | $102\ \mathrm{T/m}$ | $136\ \mathrm{T/m}$ |
| Peak field in coil | 3.328 T | 4.073 T |
| $a_6(10^{-4})$ | -0.572 | -2.018 |
| $a_{10}(10^{-4})$ | -1.762 | -1.312 |

These two racetrack quadrupole magnet examples are theoretically feasible. In our study, only two rectangular blocks were used to adjust the high-order field harmonics, and the systematic field harmonics achieved a precision of $10^{-4}$. In specific engineering applications, more rectangular blocks may be required to satisfy the design requirements. In summary, using a superconducting cable to fill the block area

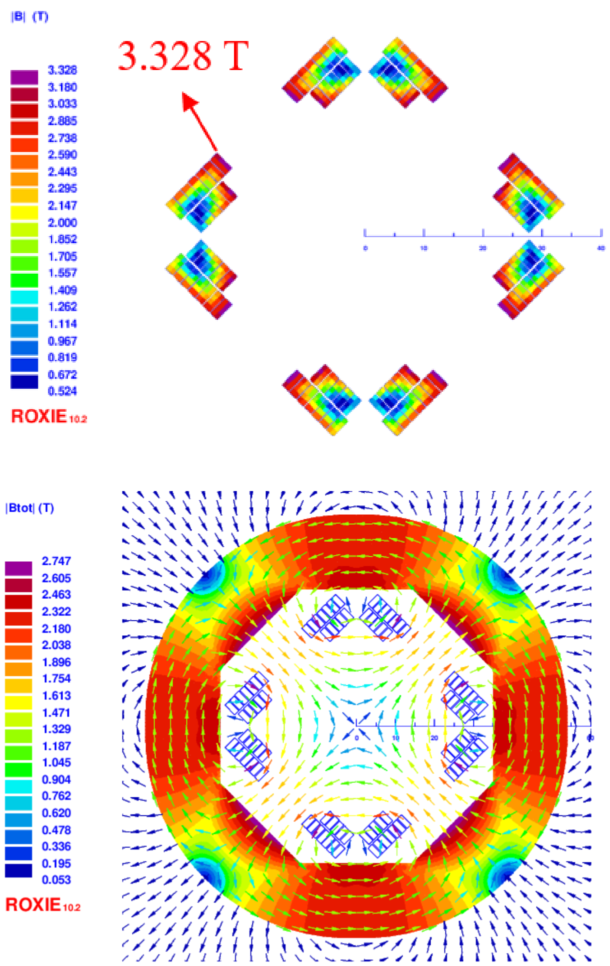


Fig. 11. Calculation model of small-aperture and high-gradient racetrack quadrupole coil

in the large-aperture high-gradient model and small-aperture high-gradient model can satisfy our design requirements, and the magnetic field quality accuracy reaches the order of $10^{-4}$. According to the superconductor critical current density curve, the peak magnetic field and current-carrying density in the racetrack coil with a large aperture and high gradient exceed the critical performance of low-temperature superconductors NbTi and $\mathrm{Nb_3Sn}$, and the isotropic high-temperature superconductor Bi-2212 is the best choice [45, 46]. Racetrack coils with small apertures and high gradients can simultaneously use both low- and high-temperature superconductors simultaneously. The advantages of using a low-temperature superconductor are that the coil structure is simple and convenient to manufacture and the operating margin of the magnet is relatively sufficient. The use of a high-temperature superconductor can further increase the operating margin, stability, and anti-interference ability of magnets.

## V. SUMMARY

Through research on a superconducting racetrack quadrupole coil, analytical formulas for high-order field harmonics and field gradients with respect to the current density and coil, geometric parameters were obtained, and the analytical numerical calculation results of the magnetic field were consistent with the finite element calculation results. A genetic algorithm was applied to obtain a solution for the coil geometry parameters with field harmonics on the order of $10^{-4}$. Finally, preliminary electromagnetic designs of large-aperture and small-aperture racetrack superconducting quadrupole magnets are presented.

The racetrack superconducting quadrupole coil had a simple shape and manufacturing process, in which both high- and low-temperature superconductors can be used. A racetrack quadrupole coil with a simple geometric structure is beneficial for strain-sensitive high-temperature superconductors and is an effective way to realize ultra-high magnetic field gradients. For low-field magnets, the use of low-temperature superconductor racetrack coils can simplify the process and reduce costs. High-temperature superconductors can also be used in low-field racetrack magnets to increase the magnet operating margin and improve magnet stability. Racetrack superconducting quadrupole magnets are a frontier research direction, and the research presented in this paper provides a new concept for the design of superconducting quadrupole magnets.

## VI. APPENDIX

Each order multipole field component $A_n$ of the entire racetrack quadrupole coil was obtained. The analytical expressions for the most important multipole field components, $A_6$ and $A_{10}$ are

$$
\begin{aligned}
A_6 = {} & \frac{4\mathrm{R}_{ref}^5 u_0 j}{5\pi}\left(\frac{6a^4+4a^2c^2+c^4}{24(a^2+c^2)^4}-\frac{6b^4+4b^2c^2+c^4}{24(b^2+c^2)^4}\right)-\frac{4\mathrm{R}_{ref}^5 u_0 j}{5\pi}\left(\frac{6a^4+4a^2d^2+d^4}{24(a^2+d^2)^4}-\frac{6b^4+4b^2d^2+d^4}{24(b^2+d^2)^4}\right) \\
& -\frac{8\mathrm{R}_{ref}^5 c^2 u_0 j}{\pi}\left(\frac{4a^2+c^2}{24(a^2+c^2)^4}-\frac{4b^2+c^2}{24(b^2+c^2)^4}\right)+\frac{8\mathrm{R}_{ref}^5 d^2 u_0 j}{\pi}\left(\frac{4a^2+d^2}{24(a^2+d^2)^4}-\frac{4b^2+d^2}{24(b^2+d^2)^4}\right) \\
& +\frac{4\mathrm{R}_{ref}^5 c^4 u_0 j}{\pi}\left(\frac{1}{8(a^2+c^2)^4}-\frac{1}{8(b^2+c^2)^4}\right)-\frac{4\mathrm{R}_{ref}^5 d^4 u_0 j}{\pi}\left(\frac{1}{8(a^2+d^2)^4}-\frac{1}{8(b^2+d^2)^4}\right)
\end{aligned}
$$

$$
\begin{aligned}
A_{10} = {} & \frac{4\mathrm{R}_{ref}^9 u_0 j}{9\pi}\left(\frac{70a^8+56a^6c^2+28a^4c^4+8a^2c^6+c^8}{560\left(a^2+c^2\right)^8}-\frac{70b^8+56b^6c^2+28b^4c^4+8b^2c^6+c^8}{560\left(b^2+c^2\right)^8}\right) \\
& -\frac{4\mathrm{R}_{ref}^9 u_0 j}{9\pi}\left(\frac{70a^8+56a^6d^2+28a^4d^4+8a^2d^6+d^8}{560\left(a^2+d^2\right)^8}-\frac{70b^8+56b^6d^2+28b^4d^4+8b^2d^6+d^8}{560\left(b^2+d^2\right)^8}\right) \\
& -\frac{112\mathrm{R}_{ref}^9 c^6 u_0 j}{3\pi}\left(\frac{8a^2+c^2}{112\left(a^2+c^2\right)^8}-\frac{8b^2+c^2}{112\left(b^2+c^2\right)^8}\right)+\frac{112\mathrm{R}_{ref}^9 d^6 u_0 j}{3\pi}\left(\frac{8a^2+d^2}{112\left(a^2+d^2\right)^8}-\frac{8b^2+d^2}{112\left(b^2+d^2\right)^8}\right) \\
& +\frac{4\mathrm{R}_{ref}^9 c^8 u_0 j}{\pi}\left(\frac{1}{16\left(a^2+c^2\right)^8}-\frac{1}{16\left(b^2+c^2\right)^8}\right)-\frac{4\mathrm{R}_{ref}^9 d^8 u_0 j}{\pi}\left(\frac{1}{16\left(a^2+d^2\right)^8}-\frac{1}{16\left(b^2+d^2\right)^8}\right) \\
& +\frac{16\mathrm{R}_{ref}^9 d^2 u_0 j}{\pi}\left(\frac{56a^6+28a^4d^2+8a^2d^4+d^6}{560\left(a^2+d^2\right)^8}-\frac{56b^6+28b^4d^2+8b^2d^4+d^6}{560\left(b^2+d^2\right)^8}\right) \\
& -\frac{16\mathrm{R}_{ref}^9 c^2 u_0 j}{\pi}\left(\frac{56a^6+28a^4c^2+8a^2c^4+c^6}{560\left(a^2+c^2\right)^8}-\frac{56b^6+28b^4c^2+8b^2c^4+c^6}{560\left(b^2+c^2\right)^8}\right) \\
& +\frac{56\mathrm{R}_{ref}^9 c^4 u_0 j}{\pi}\left(\frac{28a^4+8a^2c^2+c^4}{336\left(a^2+c^2\right)^8}-\frac{28b^4+8b^2c^2+c^4}{336\left(b^2+c^2\right)^8}\right) \\
& -\frac{56\mathrm{R}_{ref}^9 d^4 u_0 j}{\pi}\left(\frac{28a^4+8a^2d^2+d^4}{336\left(a^2+d^2\right)^8}-\frac{28b^4+8b^2d^2+d^4}{336\left(b^2+d^2\right)^8}\right)
\end{aligned}
$$


[1] L. Bottura, S. A. Gourlay, A. Yamamoto, A. V. Zlobin, Superconducting magnets for particle accelerators. IEEE Transactions on Nuclear Science **63**, 751-776 (2016). doi: 10.1109/TNS.2015.2485159

[2] L. Rossi, E. Todesco, Electromagnetic design of superconducting quadrupoles. Physical Review Special Topics-Accelerators and Beams **9**, 102401 (2006). doi: 10.1103/PhysRevSTAB.9.102401

[3] C. Shen, Y. S. Zhu, X. C. Yang, et al., Superconducting quadrupole magnet R&D in the interaction region of CEPC. International Journal of Modern Physics A **36**, 2142007 (2021). doi: 10.1142/S0217751X21420070

[4] Zhu Y, Yang X, Liang R, et al., Final focus superconducting magnets for CEPC. IEEE Transactions on Applied Superconductivity **30**, 4002105 (2020). doi: 10.1109/TASC.2020.2973110

[5] Y. W. Wang, F. Su, S. Bai, et al., Lattice design for the CEPC double ring scheme. International Journal of Modern Physics A **33**, 1840001 (2018). doi:10.1142/S0217751X18400018

[6] S. I. Bermudez, L. Fiscarelli, G. Ambrosio, et al., Magnetic Analysis of the MQXF Quadrupole for the High-Luminosity LHC. IEEE Transactions on Applied Superconductivity **83**, 064620 (2019). doi: 10.1109/TASC.2019.2897848

[7] P. Ferracin, G. Ambrosio, M. Anerella, et al., Magnet Design of the 150 mm Aperture Low-beta Quadrupoles for the High Luminosity LHC. IEEE Transactions on Applied Superconductivity **24**, 4002306 (2014). doi: 10.1109/TASC.2013.2284970

[8] B. Parker, M. Anerella, J. Escallier, et al., BNL Direct Wind Superconducting Magnets. IEEE Transactions on Applied Superconductivity **22**, 4101604 (2012). doi: 10.1109/TASC.2011.2175693

[9] B. Parker, J. Escallier, Serpentine coil topology for BNL direct wind superconducting magnets. Proceedings of the 2005 Particle Accelerator Conference, Knoxville, TN, USA, (2005). doi: 10.1109/PAC.2005.1590546

[10] Y. Z. Wu, et al., The Magnet System of the BEPCII Interaction Region. IEEE Transactions on Applied Superconductivity **20**, 360-363 (2010). doi: 10.1109/TASC.2010.2040027

[11] BEPC II Team. BEPC II: construction and commissioning. Chinese Physics C **33**, 60 (2009). doi: 10.1088/1674-1137/33/S2/016

[12] S. Farinon, R. Musenich, Biot-Savart Approach to Analytical Computation of Magnetic Fields and Forces of CCT Magnets. IEEE Transactions on Applied Superconductivity **31**, 4900308 (2021). doi: 10.1109/TASC.2021.3053346

[13] L. Zhou, R. Zhao, Y. Chen, et al., Structure Design and Analysis of Canted-Cosine-Theta (CCT) Superconducting Quadrupole Magnet. Shock and Vibration **2021**, 1-7 (2021). doi: 10.1155/2021/8895136

[14] E. M. Mei, et al., DCT&CCT Superconducting Multiplets for HIAF-HFRS. IEEE Transactions on Applied Superconductivity **32**, 4006405 (2022). doi: 10.1109/TASC.2022.3158330

[15] the FCC Collaboration (2019), FCC-ee: The Lepton Collider: Future Circular Collider Conceptual Design Report Volume 2. European Physical Journal: Special Topics **228**, 261-623 (2019). doi: 10.1140/epjst/e2019-900045-4

[16] W. J. Yang, L. Z. Ma, J. Yang, et al., A magnetic field measurement system of superconducting quadrupole for linear accelerator. Journal of Instrumentation **15**, T12007 (2020). doi: 10.1088/1748-0221/15/12/T12007

[17] E. Cho, H. Mueller, K. Sugita, et al., Preliminary Test Results of the First of Series Multiplet for the Super-FRS at FAIR. IEEE Transactions on Applied Superconductivity **30**, 4101504 (2020). doi: 10.1109/TASC.2020.2981302

[18] Xian Jing Sun, Fu San Chen, Xiang Chen Yang, et al., Superconducting multipole wiggler with large magnetic gap for

HEPS-TF. Nuclear Science and Techniques **33**, 16 (2022). doi: 10.1007/s41365-022-01001-5

[19] Ya Zhu, Qinglei Zhang, Qiaogen Zhou, Design and verification of a novel high gradient quadrupole magnet. Nuclear Techniques **45**, 070102 (2022). doi: 10.11889/j.0253-3219.2022.hjs.45.070102

[20] Chan Liu, Jidong Zhang, Qiaogen Zhou, A small aperture quadrupole magnet measurement method based on the single stretched wire method. Nuclear Techniques **46**, 060201 (2023). doi: 10.11889/j.0253-3219.2023.hjs.46.060201

[21] R. Gupta, M. Anerella, J. Cozzolino, G. Ganetis, et al., Second Generation HTS Quadrupole for FRIB. IEEE Transactions on Applied Superconductivity **21**, 1888-1891 (2011). doi: 10.1109/TASC.2010.2091247

[22] P. Ferracin, G. Ambrosio, E. Barzi, et al., Assembly and tests of SQ02, a Nb3Sn racetrack quadrupole magnet for LARP. IEEE Transactions on Applied Superconductivity **17**, 1019-1022 (2007). doi: 10.1103/PhysRevC.89.057602

[23] P. Ferracin, S. E. Bartlett, S. Caspi, D. R. Dietderich, et al., Development of a large aperture Nb3Sn racetrack quadrupole magnet. IEEE Transactions on Applied Superconductivity **15**, 1132-1135 (2005). doi: 10.1109/TASC.2005.849511

[24] R. Gupta, M. Anerella, J. Cozzolino, B. Parker, et al., Modular High Field Quadrupole Design for Electron-Ion Collider. IEEE Transactions on Applied Superconductivity **29**, 4001505 (2019). doi: 10.1109/TASC.2019.2896376

[25] G. Baek, J. Kim, S. Han, et al., Effect of Screening Current Induced Field on Field Quality of an Air-Core HTS Quadrupole Magnet. IEEE Transactions on Applied Superconductivity **30**, 4602304 (2020). doi: 10.1109/TASC.2020.2979842

[26] R. Gupta, Modular design and modular program for high gradient quadrupoles. IEEE Transactions on Applied Superconductivity **17**, 1273-1276 (2007). doi: 10.1109/TASC.2007.898141

[27] Y. S. Zhu, Y. Z. Wu, W. Kang, Magnetic Field Simulation of Serpentine Quadrupole Coil, IEEE Transactions on Applied Superconductivity **22**, 4901105 (2012). doi: 10.1109/TASC.2011.2177623

[28] C. Shen, Y. S. Zhu, F. S. Chen, Magnetic design study of coil-dominated superconducting quadrupole magnets based on racetrack coils. arXiv preprint arXiv:2108.11643, 2021. doi: 10.48550/arXiv.2108.11643

[29] R. A. Beth, Complex representation and computation of two-dimensional magnetic fields. Journal of Applied Physics. **7**, 2568-2571 (1966). doi: 10.1063/1.1782086R

[30] S. Bai, C. Yu, Y. W. Wang, et al., Accelerator physics design in the interaction region for CEPC double ring scheme. International Journal of Modern Physics A **34**, 1940002 (2019). doi: 10.1142/S0217751X19400025

[31] J. Gao, CEPC and SppC Status—From the completion of CDR towards TDR. International Journal of Modern Physics A **36**, 2142005 (2021). doi: 10.1142/S0217751X21420057

[32] G. Sun, Y. Tian, R. Wang, et al., Parallelized multi-objective efficient global optimization algorithm and its applications. Structural and Multidisciplinary Optimization **61**, 763-786 (2020). doi: 10.1007/s00158-019-02417-1

[33] J. Blank, K. Deb, Pymoo: Multi-Objective Optimization in Python. IEEE Access **8**, 89497-89509 (2020). doi: 10.1109/ACCESS.2020.2990567

[34] G. Dhiman, K. K. Singh, A. Slowik, et al., EMoSOA: a new evolutionary multi-objective seagull optimization algorithm for global optimization. International Journal of Machine Learning and Cybernetics **12**, 571-596 (2021). doi: 10.1007/s13042-020-01189-1

[35] C. Gil, A. Márquez, R. Baños, et al., A hybrid method for solving multi-objective global optimization problems. Journal of Global Optimization **38**, 265-281 (2007). doi: 10.1007/s10898-006-9105-1

[36] P. Ferracin, G. Ambrosio, M. Anerella, A. Ballarino, et al., Development of MQXF: The $\mathrm{Nb_3Sn}$ Low-$\beta$ Quadrupole for the Hi-Lumi LHC. IEEE Transactions on Applied Superconductivity **26**, 4000207 (2016). doi: 10.1109/TASC.2015.2510508

[37] M. Juchno, G. Ambrosio, M. Anerella, D. Cheng, et al., Support Structure Design of the $\mathrm{Nb_3Sn}$ Quadrupole for the High Luminosity LHC. IEEE Transactions on Applied Superconductivity **25**, 4001804 (2015). doi: 10.1109/TASC.2014.2366034

[38] D. K. Namburi, Y. Shi, D. A. Cardwell, The processing and properties of bulk (RE)BCO high temperature superconductors: current status and future perspectives. Superconductor Science and Technology **34**, 053002 (2021). doi: 10.1088/1361-6668/abde88

[39] D. Uglietti, A review of commercial high temperature superconducting materials for large magnets: from wires and tapes to cables and conductors. Superconductor Science and Technology **32**, 053001 (2019). doi: 10.1088/1361-6668/ab06a2

[40] CEPC Study Group, CEPC conceptual design report: Volume 1-accelerator. arXiv preprint arXiv:1809.00285, 2018. doi: 10.48550/arXiv.1809.00285

[41] Hong Juan Zheng, Jie Gao, Ji Yuan Zhai, et al., RF design of 650 MHz 2-cell cavity for CEPC collider. Nuclear Science and Techniques **30**, 155 (2019). doi: 10.1007/s41365-019-0671-6

[42] Peng Sha, Wei Min Pan, Song Jin, et al., Ultrahigh accelerating gradient and quality factor of CEPC 650 MHz superconducting radio-frequency cavity. Nuclear Science and Techniques **33**, 125 (2022). doi: 10.1007/s41365-022-01109-8

[43] Mei Yang, Fu San Chen, Ya Feng Wu, et al., Development of short prototype of dual aperture quadrupole magnet for CEPC ring. Nuclear Science and Techniques **34**, 103 (2023). doi: 10.1007/s41365-023-01255-7

[44] C. Shen, Y. S. Zhu, F. S. Chen. Design and Optimization of the Superconducting Quadrupole Magnet Q1a in CEPC Interaction Region. IEEE Transactions on Applied Superconductivity **32**, 4004804 (2022). doi: 10.1109/TASC.2022.3163684

[45] T. Shen, L. G. Fajardo, Superconducting accelerator magnets based on high-temperature superconducting Bi-2212 round wires. Instruments **4**, 4020017 (2020). doi: 10.3390/instruments4020017

[46] S. C. Kim, D. W. Ha, S. S. Oh, K. J. Song, et al., Fabrication and properties of Bi2212 Rutherford superconducting cable. IEEE Transactions on Applied Superconductivity **19**, 3076-3079 (2009). doi: 10.1109/TASC.2009.2018852